Microstructure tailoring of Al-containing compositionally complex alloys by controlling the sequence of precipitation and ordering

Stephan Laube[a], Steven Schellert[b], Aditya Srinivasan Tirunilai[a], Daniel Schliephake[a], Bronislava Gorr[a], Hans-Juergen Christ[b], Alexander Kauffmann[a,*] and Martin Heilmaier[a]

[a] Institute for Applied Materials (IAM), Karlsruhe Institute of Technology (KIT), Engelbert-Arnold-Str. 4, 76131 Karlsruhe, Germany

[b] Institut für Werkstofftechnik, Universität Siegen, Paul-Bonatz-Str. 9-11, 57068 Siegen, Germany

* corresponding author
mail: alexander.kauffmann@kit.edu (A. Kauffmann)
phone: +49 721 608 42346

Highlights (3 to 5 Bullet points, max. 85 Characters per Bullet point)

- Refractory metal-based compositionally complex alloys exhibit a two-phase microstructure.
- The room temperature crystal structure can be tailored by the phase transition sequence.
- Differential scanning calorimetry reveals both, order reaction and phase separation.
- The Al concentration has a significant influence on the order reaction.

Abstract (222 / 250 words)

Refractory metal-based, Al-containing compositionally complex alloys (RCCA) are promising candidates for high-temperature structural applications. To shed light on the complex phase transitions, thermodynamic calculations were performed to select two representative alloys with different sequences in phase transitions. Samples of these compositions were synthesized by arc melting of pure elements followed by a homogenization treatment to experimentally verify the room temperature microstructure and assess the phase transitions. Differential scanning calorimetry (DSC), scanning (SEM) and transmission electron microscopy (TEM) studies after the homogenization and quenching revealed multiple distinct sequences of transitions: (i) 82(TaMoTi)-8Cr-10Al (in at.%) exhibits a solid-state phase separation concurrent with ordering of the precipitates. This results in a disordered matrix with ordered precipitates. Thermal analysis indicates that while cooling from the high-temperature A2 phase, the phase separation and ordering are spread out over a large temperature range (approx. 750 – 1250 °C), with a peak at 1055 °C. (ii) In the 77(TaMoTi)-8Cr-15Al alloy, a continuous phase transition at 1155 °C leads to a single-phase B2 matrix with planar faults. At slightly lower temperatures (approx. 1094 °C) phase separation occurs, resulting in a B2 matrix with segregation at planar faults and A2 precipitates. In both investigated compositions, the A2 phase is enriched in Ta and Mo. Conversely, the B2 phase is enriched in Al and Ti, while Cr is uniformly distributed in the phases.

Keywords (6 / 6 words)

Refractory compositionally complex alloys (RCCA); Refractory high entropy alloy (RHEA); phase transition; crystal structure; differential scanning calorimetry (DSC); transmission electron microscopy (TEM)

1 Introduction

Refractory complex concentrated alloys (RCCA) have garnered significant scientific interest in the previous decade [1, 2, 3, 4, 5]. From an engineering perspective, the alloys are plausible candidates for high-temperature structural applications. Several reported RCCA have potential application temperatures and strength that go beyond the currently used alloys [6, 7]. Additionally, they provide the possibility of investigating high-temperature deformation as well as strengthening mechanisms in concentrated solid solutions with body-centered cubic (BCC) crystal structure. However, this set of attractive characteristics comes with some disadvantages. Many alloy compositions consisting only of refractory elements exhibit (i) high densities and (ii) insufficient oxidation resistance, precluding their use for high-temperature application in air [8, 9, 10]. Therefore, many RCCA reportedly contain some lighter elements, which are known to form protective oxide scales, e.g., Cr, Al [11, 12], and increase the specific material properties, e.g., Ti or Al [13]. Experimental results further promote the idea that some carefully selected RCCA exhibit excellent oxidation resistance [10, 14, 11, 15, 16, 17]. However, the resultant consequence of promising oxidation resistance is that many of the lighter elements form intermetallic phases with other elements, compromising ductility and toughness, especially at room temperature. Furthermore, the formation of additional complex phases makes it complicated to unambiguously identify the deformation mechanisms in RCCA.

Apart from the aforementioned tradeoff between the formation of complex secondary phases and oxidation resistance and density decrease, an additional point has to be considered: many reported RCCA exhibit brittle behavior at lower temperatures (e.g., room temperature) [3]. The origin of the brittleness has been linked to ordered crystal structures in some RCCA. It has been seen that light elements, apart from their tendency to form intermetallic phases, are predominantly responsible for the ordering in these alloys. Recent investigations have highlighted the importance of Al in controlling possible ordered phases at lower temperatures [1, 18, 19, 20]. In studies on the Nb-Ta-Mo-Ti-Cr-Al system [19], it was revealed that an expectedly continuous order transition from a high-temperature disordered BCC crystal structure (*Strukturbericht* A2, W prototype) to a low temperature ordered BCC (*Strukturbericht* B2, CsCl prototype) crystal structure takes place. The critical temperatures of these phase transitions strongly depend on alloy composition [19]. In the present case of alloys from the Mo-Ti-Cr-Al system, it has been shown that the order-disorder transition temperature is dictated by Al concentration [18].

The tendency of Al to promote order can be utilized to establish microstructures with a suitable distribution of ordered and disordered phases with the objective of achieving favorable high-temperature properties of the alloys. As is known from classical high-temperature materials like Ni-based superalloys, a two-phase microstructure consisting of a disordered matrix with ordered, coherent precipitates is desirable for high-temperature application (e.g., high resistance against creep deformation) while maintaining acceptable room temperature ductility and toughness [21]. A similar effect may be presently mimicked in alloys of the Mo-Ti-Cr-Al system. However, it is important to note, that this is not a trivial task, as A2 and especially B2 alloys are known to be brittle at room temperature. Some RCCA exhibit significant ductility at room temperature, but the appropriate compositions for this are not readily obvious [3]. Apart from this, owing to the lower packing factor (in comparison to A1 and

$L1_2$) dislocation-based plasticity is strongly depending on temperature which also leads to temperature-depending ductility. Nevertheless, higher absolute solidus and solvus temperatures linked to these alloys might help to achieve a comparably similar resistance against creep deformation. Based on this discussion it is apparent, that while A2-B2 two-phase systems likely have potential for high-temperature applications in terms of possible oxidation and creep resistance, but they may sacrifice room and high-temperature ductility.

Several RCCA and high entropy alloys (HEA) with a two-phase microstructure were investigated in past years [1, 2]. A similar but inverted microstructural combination was investigated in the Al-Co-Cr-Fe-Ni-Cu system by Santodonato and co-workers [22, 23]. The stable phases at room temperature are a B2 matrix phase consisting of primarily Ni and Al as well as A2 precipitates consisting primarily of Fe and Cr. Through variation of the Al concentration, the order parameter and the onset temperature of ordering were changed. However, for compositions with high Al concentrations, no disordered high-temperature phase was observed. Jensen et al. [3, 24, 25] characterized, in detail, the composition 80(AlNbTiZr)-20(TaMo) (in at.%). This exhibits a similar microstructure consisting of a B2 matrix with coherent, cuboidal A2 precipitates forming a basketweave structure inside the grains. Therein, the disordered precipitates are surrounded by thin continuous B2 channels. This microstructure exhibits a compression yield strength $\sigma_{0.2}$ at 1000 °C of approx. 745 MPa [25]. However, the strain to fracture at room temperature (RT) is below 10 % in compression (with approx. $\sigma_{0.2}$ = 2000 MPa at RT). Therefore, no significant tensile plasticity is expected at RT. A possible but limited method of attaining a disordered matrix was demonstrated by Soni et al. [26] for an alloy from the Al-Nb-Ta-Ti-V-Zr system. The alloy separates via spinodal decomposition from a high temperature disordered single-phase structure into a continuous B2 matrix with A2 precipitates. A phase inversion by prolonged annealing at 600 °C was reported. It was assumed that this phenomenon is driven by reducing the interface and elastic strain energy of the system [26].

Conclusively, the mechanical properties of two-phase, Al-containing RCCA seem promising in comparison to conventional high temperature engineering alloys but they are saddled by some problematic points, which if addressed would be greatly beneficial in designing and synthesizing superior high-temperature alloys in the future. Among these issues are: (i) the phase compositions of Al-containing RCCA are hard to predict. While most of them exhibit B2 ordering, only a few of the binary alloys with Al exhibits the B2 crystal structure [27, 28, 29, 30]. Correspondingly, there is still a necessity for holistic rules to predict the formation in higher-order systems. (ii) The matrix phase is predominantly ordered in the reported alloys and the reaction pathways are hardly ever investigated and thus still prove elusive. (iii) Other meaningful properties for high temperature structural applications, like creep and corrosion have rarely been examined so far.

Therefore, non-equimolar RCCA were investigated in this study in order to further strengthen the understanding of the phase transitions. Alloys from the Ta-Mo-Ti-Cr-Al systems with lower Cr and Al concentrations with respect to the equimolar RCCA were chosen as appropriate candidates for investigation. In comparison to the equimolar composition, the Cr content was significantly modified to avoid the formation of a substantial amount of secondary phases (in particular the Laves phase, according to Ref. [31, 32]). The Al concentration was carefully varied based on preceding thermodynamic calculations. Furthermore, a specific focus was placed on the sequence of the continuous and discontinuous phase transitions.

2 Experimental and materials

The investigated alloys, referred to as 82(TaMoTi)-8Cr-10Al and 77(TaMoTi)-8Cr-15Al (in at.%), were produced by repetitive arc melting in Ar atmosphere. The utilized bulk elements (provided by chemPUR GmbH, Germany), Ta, Mo, Ti, Cr and Al had purities of 99.9, 99.95, 99.8, 99.99 and 99.99%, respectively. Through the process of multiple melting operations, at least five in each case, buttons of approximately 120 g in weight were synthesized. Subsequently, the buttons were cast into a cuboidal shape. Further details regarding the manufacturing process are stated elsewhere [19]. In order to ensure chemical homogeneity, the samples were heat treated at 1600 °C for a dwell time of 20 h utilizing an HTRT 70-600/18 resistance tube furnace by Carbolite Gero GmbH & Co. KG (Germany). To prevent oxidation, the tube furnace was evacuated and backfilled with Ar three times before establishing a continuously flowing high-purity Ar atmosphere. The heating and cooling were performed at 250 K/h. Samples for quenching experiments were extracted from the 1600 °C heat treated material and encapsulated in fused-silica ampoules (evacuated and backfilled with high-purity Ar). The heat treatments were conducted inside an L3/S27 resistance furnace by Nabertherm (Germany) for 30 min. The quenching was performed by breaking the ampoules submerged in water.

Samples for microstructural investigation were first ground using SiC papers, followed by metallographic polishing with 3 µm and 1 µm polycrystalline diamond suspensions. Subsequently, the samples were etched for 5 min using a reagent consisting of NH_3, H_2O_2 and distilled water in a 1:2:5 ratio. The final surface was chemo-mechanically vibratory polished for at least 12 h with a polishing suspension supplied by Struers (Germany), which is stabilized at a pH of 9.8.

The chemical composition was verified by inductively coupled plasma-optical emission spectrometry (ICP-OES) for 82(TaMoTi)-8Cr-10Al and standard-related energy-dispersive X-ray spectroscopy (EDS) using a Zeiss EVO50 from Carl Zeiss AG (Germany). EDS was performed with a silicon drift detector by Thermo Fisher Scientific Inc. (USA) at an acceleration voltage of 30 kV. The 82(TaMoTi)-8Cr-10Al sample and the ICP-OES result for it served as reference for the EDS on 77(TaMoTi)-8Cr-15Al. Further microstructural investigations were carried out by means of scanning electron microscopy (SEM) using a Helios NanoLab™ 650 from Thermo Fisher Scientific Inc. by utilizing its Backscatter Electron (BSE) detector and an X-Max detector by Oxford Instruments (England) for further EDS measurements (with 30 kV acceleration voltage).

A Talos F200X by Thermo Fisher Scientific Inc. was used for electron diffraction experiments. The Transmission Electron Microscope (TEM) was operated at an acceleration voltage of 200 kV. Selected Area Diffraction (SAD) pattern, Dark-Field (DF) as well as High-Angle Annular Dark-Field (HAADF) micrographs were recorded. The thin foils were prepared from bulk specimens. First, a sample was cut using a wire saw and then mechanically ground with SiC paper to about 100 µm thickness. Subsequently, the samples were thinned until finally perforated by a TenuPol-5 electrolytic polishing device provided by Struers GmbH. A potential of 12 V was applied at room temperature and the electrolyte was composed of H_2SO_4 and CH_3OH, mixed in a 4:1 ratio.

X-ray diffraction (XRD) was performed on powder specimens (particle size <40 µm) utilizing an X'Pert Pro MPD diffractometer by Malvern Panalytical B.V. (Netherlands). The powder specimens were obtained by crushing bulk material with an agate mortal, followed by sieving with a 40 µm sieve. The scanning was performed in a Bragg-Brentano geometry with Cu-Kα radiation. The step size in 2Θ was 0.005° with an accumulated acquisition time per step of 500 s per step. Further details regarding the acquisition and evaluation of the XRD data are stated elsewhere [18, 31]. Additional experiments on un-sieved, crushed material did not reveal significant differences in peak position. Sieving ensures

statistical relevance of the determined peak intensity ratios. The density was determined by the Archimedes' principle with a ME204T scale by Mettler-Toledo GmbH (Switzerland).

To detect possible order reactions, the samples were investigated by means of high-temperature differential scanning calorimetry (DSC). $\mathrm{d}H/\mathrm{d}T$ was determined utilizing a DSC 404 F1 Pegasus® provided by Netzsch-Gerätebau GmbH (Germany) equipped with an A54 sample holder (with a type S-thermocouple) and a high-temperature Pt-furnace. Samples with disk shape were cut by electrical discharge machining from bulk material with a diameter of 5 to 6 mm and a height of approximately 1 mm. All surfaces were ground by SiC paper. One surface was ground up to grit size P4000 to ensure a smooth and planar surface for contact with the pan. Samples were tested inside a Pt-crucible with an Al_2O_3 inlet and a Pt-lid. The measurements were performed at a heating rate of 10, 20 and 40 K/min after holding at 200 °C for 30 min. Each composition was tested at least three times. To prevent oxidation, a Zr getter was placed in the vicinity of the sample and the measurement was performed in a flowing Ar atmosphere with a purity of 99.9999 %, provided by Air Liquide S.A. (France). The recorded signal was corrected for the baseline signal of the empty pan. To determine $\mathrm{d}H/\mathrm{d}T$ a reference sapphire sample from Netzsch with a similar mass as the RCCA samples was measured and evaluated according to DIN 51007. The device was temperature calibrated according to Ref. [33] with the provided calibrating set from Netzsch. By thermal cycling inside the DSC, samples of the two compositions were first investigated, to see whether the measured thermal signature is reproducible and whether the transition is enantiotropic (reversible transition to another phase of the same chemical composition). After confirming the reversibility, only a single sample was investigated for all heating rates. The position of the Pt/Rh pans was not changed in the series of consecutive measurements [33]. However, due to the inevitable position change of the pans after sample change, small measurement artifacts are observed and marked by * in Fig. 5.

Table 1: Determined chemical composition $\overline{x}$ of the investigated alloys, given in at.%. ICP-OES is indicated by * and standard-related EDS by †.

abbreviation	desired composition / at.%	$\overline{x}$ / at%				
		Ta	Mo	Ti	Cr	Al
82(TaMoTi)-8Cr-10Al†	27.3Ta-27.3Mo-27.3Ti-8Cr-10Al	27.3	26.6	28.8	7.1	10.1
77(TaMoTi)-8Cr-15Al*	25.6Ta-25.6Mo-25.6Ti-8Cr-15Al	26.4	27.0	26.3	7.1	13.2

3 Thermodynamic calculations

Examinations of Al-containing RCCA indicated that Al has a significant influence on the ordering and possible intermetallic phases in these alloys [18, 19, 34]. The thermodynamic calculations discussed here, were performed using FactSage V7.2 with an in-house database [31]. The database for the system Ta-Nb-Mo-Cr-Ti-Al is based on the FRAN database (including Mo, Cr, Ti and Al) by GTT-Technologies (Germany) and was extended by the missing elements Nb and Ta. Further information is provided in the Supplemental. The calculations predict a two-phase microstructure consisting of A2 + B2 at lower temperatures for both the investigated alloys. For visual assessment, a quasi-binary phase diagram is depicted in Fig. 1, with a variation of the atomic concentration of Al from 0 to 30 at.%. In this compositional range, a Laves phase (*Strukturbericht* C15) is predicted. However, the predicted absolute phase percentage is low with a maximum of 12% at 600 °C. At other temperatures, the phase fractions significantly decrease. The Laves phase is omitted from further consideration due to its expected low participation and/or influence on the phase transitions under investigation [19].

Furthermore, this phase was not found in the present samples to a substantial amount (less than 0.1 vol.%).

Below 2.5 at.% Al, a low-temperature phase transition is not anticipated, although, it may occur at temperatures lower than the calculated range (the lower boundary for the thermodynamic calculation was set to 300 °C). To further verify the result of the thermodynamic calculation, an Al-free alloy was synthesized (in the same way as stated above) and investigated by various methods to confirm that no phase transition occurs and the alloy is single-phase A2 at room temperature (further information is depicted in Supplemental Fig. S1). The high temperature disordered phase is expected to be stable throughout the entire investigated temperature range for alloys with less than 2.5 at.% Al. For more than 12.5 at.% Al, a B2 phase field is anticipated at intermediate temperatures (between approximately 500 and 1000 °C). The ordering temperature seems to be quite sensitive to the Al concentration, changing from 750 °C for 15 at.% to above 1000 °C for 25 at.%. In contrast, the boundary between B2 and A2 + B2 is in the range of 550 °C to 700 °C and does not feature a strong correlation with the Al concentration. It should be noted here that, based on Ref. [18], the calculated temperatures are expected to be lower than experimentally observed.

The investigations discussed within this article will focus on two compositions indicated by vertical lines in Fig. 1. These two compositions were chosen because the predicted phase transitions differ significantly from one another, despite having fairly similar compositions. For 82(TaMoTi)-8Cr-10Al, a single-phase transition is estimated at around 600 °C, from the high-temperature phase A2 to the low-temperature phases A2 + B2. In the case of 77(TaMoTi)-8Cr-15Al, two phase transitions are proposed: one at 750 °C, ordering from A2 to B2 and one at 650 °C from B2 to B2 + A2. The temperature-dependent compositions of the phases are provided in the Supplemental Fig. S2. In the investigated alloys, the compositions of the phases are similar and, therefore, summarized for both. In comparison to the alloy's composition, the A2 phase is enriched in Ta and Mo (35 – 45 at.%), while depleted in Ti, Cr and Al with approx. 14, < 1 and 3 at.%, respectively. Hence, the B2 phase consists of a significant amount of Ti, Cr and Al with 20, 8 and 12 at.%, respectively. For Ta and Mo, concentrations of 3 at.% (Ta) and < 1 at.% (Mo) are calculated in the B2 phase.

Due to the restrictions of thermodynamic calculations, no definitive statement on the type of the matrix and the precipitates can be made. The calculations merely provide guidance with respect to the trend and illustrate the possible phase transitions; however, the physical sequence of reaction is not certain. Within this system, several sequences are possible in principle, which may lead to a similar microstructure at room temperature [35]. In order to describe the sequences, two distinct reactions have to be assessed: (i) the type and temperature of phase separation (transition with a composition change) and (ii) the ordering transition at the ordering temperature (ordering temperature, denoted by T_c, and critical temperature will be used interchangeably here). Depending on the alloy composition, these may vary significantly or even overlap. In the following paragraphs, the two steps are described in general and then transferred to the present system.

The following types of solid-state transitions with the different phases α, β and γ are possible during cooling [36, 37]: (i) peritectoid reaction: $\alpha + \beta \rightarrow \gamma$; (ii) eutectoid reaction: $\gamma \rightarrow \alpha + \beta$; (iii) precipitation with nucleation and growth of β from α: $\alpha \rightarrow \alpha + \beta$; (iv) spinodal decomposition from a homogeneous solution α: $\alpha \rightarrow \alpha_1 + \alpha_2$ where α_1 and α_2 denote different chemical compositions of the phase α. Magnetic, shear and other transitions with structural and/or without compositional changes are omitted for the sake of clarity. Peritectoid and eutectoid reactions can be ruled out, because they exhibit a distinct set of features, which can be experimentally distinguished (discontinuous transition with an

inhomogeneous reaction kinetic), but which is not seen here as elaborated by the DSC results further below. Hence, the possibilities for phase separation are either through spinodal decomposition as a continuous reaction with no energetic barrier or discontinuous precipitation with an energetic barrier and a sharp interface [36, 37, 38].

Because the ordered B2 phase has only two distinct lattice sites, it is not feasible to arrange all five elements of the investigated alloy on a separate lattice site [19]. Either some lattice sites are left vacant or some atoms need to be located on either site. In the general case of alloys with non-stoichiometric composition or an uneven number of elements, the respective site occupation is not trivial and, thus, out of the scope of this paper. However, another characteristic associated with the order transition $\alpha \rightarrow \alpha'$, with α' being the ordered phase of α, is, whether the degree of order changes continuously (e.g., over a temperature interval, an example for this is CuZn) or discontinuously (e.g., at an exact temperature, an example is Cu_3Au) [37]. The different thermodynamic characteristic of the ordering lead to different temperature dependences of the Gibbs free energies G and enthalpies H close to T_c [39, 36]. While G and H are not directly accessible by experiments, the derivative $\mathrm{d}H/\mathrm{d}T$ can be obtained by means of calorimetry [40].

When accounting for the ordering at T_c, this can lead to different resulting reaction pathways. A phase resulting from phase separation of a certain kind at $T_{\mathrm{separation}}$ can instantly undergo ordering during formation if the ordering temperature of the respective composition is above the separation temperature ($T_c \geq T_{\mathrm{separation}}$) or subsequent to separation if the temperature is below ($T_c < T_{\mathrm{separation}}$).

As depicted in Fig. 1, the sequence from an A2 crystal structure at high temperatures to A2 and B2 at low temperatures is predicted for the Al concentration range from 2.5 at.% to 12.5 at.%. At higher Al concentrations, the pathway A2 to B2 at high temperature and finally to B2 + A2 is anticipated during cooling. Whether the transitions from single- to dual-phase microstructure occur through spinodal decomposition or precipitation and at which temperatures ordering occurs is unclear. In principle, the following two sequences for cooling from high to low temperatures are possible for 82(TaMoTi)-8Cr-10Al: $\alpha \rightarrow \alpha_1 + \alpha'_2$ via spinodal decomposition or $\alpha \rightarrow \alpha + \beta'$ by precipitation, both accompanied with (almost) simultaneous ordering (note that for the case of precipitation also ordering of the matrix can occur). For 77(TaMoTi)-8Cr-15Al, $\alpha \rightarrow \alpha' \rightarrow \alpha'_1 + \alpha_2$ or $\alpha \rightarrow \alpha' \rightarrow \alpha' + \beta$ with ordering takes place at high temperatures first and spinodal decomposition or precipitation occurs at low temperatures. However, in order to make a distinct statement on the phase transition pathway in each case experimental evidence is necessary.

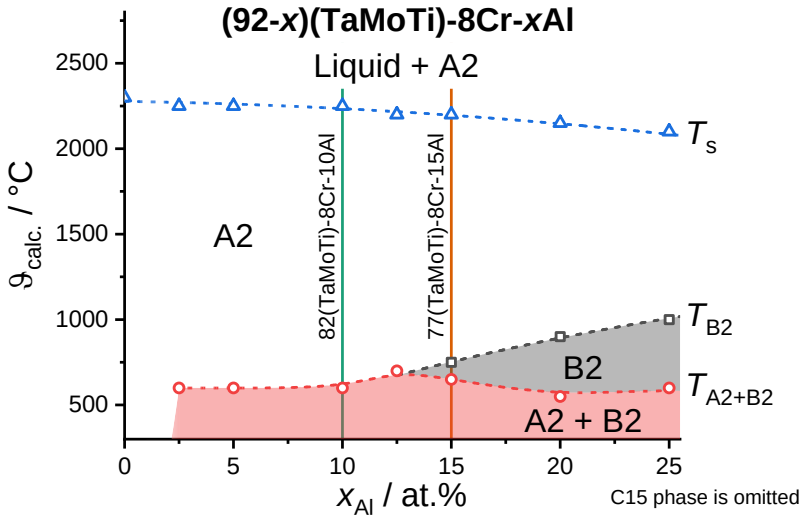

Fig. 1. Equilibrium phases as calculated by FactSage as a function of temperature ϑ and concentrations of Al x_{Al} (given in at.%) for (92-x_{Al})(TaMoTi)-8Cr-x_{Al}Al. The minor C15 Laves phase fraction is omitted for sake of clarity. The calculations had a step size of 25 K in temperature and between 2.5 at.% and 5 at.% per concentration step. The schematic phase diagram includes the predicted solidus temperature T_{s} (in blue and open triangles) as well as the transition temperature T_{B2} from the A2 to the B2 crystal structure (in gray and with open squares). $T_{\mathrm{A2+B2}}$ for the transition toward a dual-phase microstructure is marked by the red dashed line and open circles. Please note that the dotted lines are to guide the eyes.

251

4 Experimental results

To ensure that the as-cast dendritic microstructure does not affect further experimental investigations, the alloys were homogenized at 1600 °C for 20 h after arc melting. The chemical composition of the manufactured alloys is given in Table 1 and was checked by means of ICP-OES and standard-related EDS. The experimentally observed compositions are in good agreement with the desired compositions. However, a slight depletion of Cr throughout the samples was determined as well as a slight depletion of Al in case of the 77(TaMoTi)-8Cr-15Al alloy. The respective lattice parameters are 0.3196 nm for 82(TaMoTi)-8Cr-10Al and 0.3189 nm for 77(TaMoTi)-8Cr-15Al (determined by means of XRD and depicted in Supplemental Fig. S3). The experimentally determined densities are 9.8 and 9.3 g/cm³ for 82(TaMoTi)-8Cr-10Al and 77(TaMoTi)-8Cr-15Al, respectively.

The orientation contrast micrographs in Fig. 2 display that the alloys have a coarse-grained microstructure. The alloys exhibit porosity within the grains, which is seen as dark features in the orientation contrast micrographs, as expected from the laboratory-scale casting process and the likely appearance of the Kirkendall effect during homogenization [41]. No remaining chemical contrast of the prior dendritic microstructure could be identified. The corresponding EDS maps of the respective elements are also depicted in Fig. 2. The element maps indicate a uniform element distribution within the analyzed regions. It is expected that all samples are chemically homogeneous on the µm-scale across multiple grains. A minor amount of a secondary phase was observed along the grain boundaries and inside the grains, with less than 0.1 vol.%. The length of this lenticular, dark secondary phase is 2 to 5 µm. The remainder of the grain boundary appears slightly bright in the micrograph, which is related to atomic contrast. SEM- and STEM-EDS investigations (not shown here) indicate that the dark features are TiN resulting from N contamination during arc melting and homogenization, while rare bright features on grain boundaries can be assigned to the Laves phase. The modification of Laves phase has not been determined over the course of the present study due to its low volume fraction.

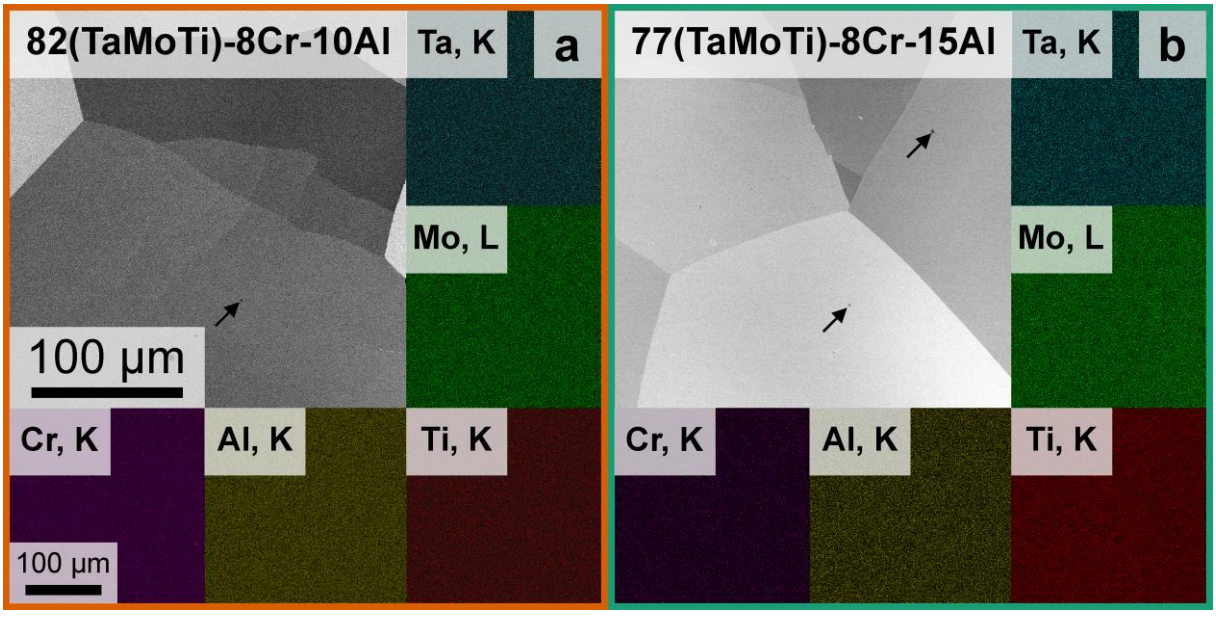

Fig. 2. BSE (orientation contrast) and EDS micrographs in the as-homogenized state of: a) 82(TaMoTi)-8Cr-10Al and b) 77(TaMoTi)-8Cr-15Al. The same magnification is used for the micrographs and the respective element maps display the same field of view as their corresponding BSE image. Black, spherical features are pores from casting and homogenization and are highlighted by arrows.

High-magnification SEM investigations were performed to confirm the phase separation and to further clarify the characteristics. As seen in Fig. 3, the microstructure on the nm-scale of the samples is

different. To confirm that the observed contrast variations within a single grain are due to different mean atomic numbers (Z-contrast), grain boundaries (for orientation contrast) and topology (by SE-contrast imaging) were carefully reviewed. To highlight the different phases, one half of each image is color-coded based on the greyscale value (assuming two distinct phases with different grey level, performed by an in-house Matlab code (The MathWorks, Inc., USA) coloring connected regions of one phase by "warm" colors (yellow to red) and one by "cold" colors (green to blue), according to Ref. [42]). 82(TaMoTi)-8Cr-10Al exhibits a strong atomic contrast through a dual-phase microstructure (Fig. 3 a)). A continuous matrix phase is present with a high BSE signal (color-coded in single green and therefore, interconnected throughout the entire image). The spacing between the phases is approximately 20 – 50 nm. The matrix phase has an area percentage of approximately 70%. In the case of 77(TaMoTi)-8Cr-15Al, the continuous matrix phase exhibits a low BSE signal and has an area percentage of roughly 55% in the micrographs. An additional feature is seen, apart from a fine two-phase microstructure (with roughly 10 – 20 nm in diameter in case of the cuboidal precipitations). Bright, loop-like features are observed utilizing SEM (see Fig. 3 b). These loops have a width of about 20 nm and manifest themselves in random orientations with a high degree of curvature. Some end at the grain boundaries and they do not intersect with other loops. A strong BSE signal indicates a higher atomic number, which reveals that the bright phase is enriched in Ta and Mo and correspondingly the dark phase could be enriched in Al, Ti and Cr. However, the micrographs yield no information about the magnitude of separation.

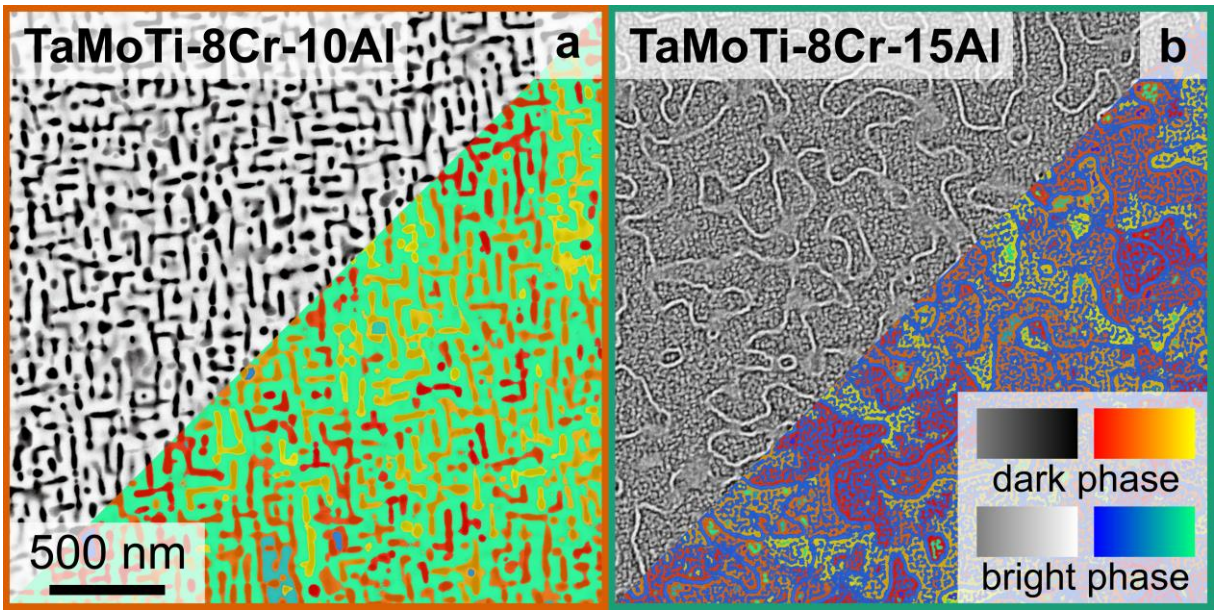

Fig. 3. BSE micrographs in the as-homogenized state of: a) 82(TaMoTi)-8Cr-10Al and b) 77(TaMoTi)-8Cr-15Al. The same magnification is used for both micrographs. The color-coded part of the images represents the result of a pixel connectivity analysis based on the binarized images. Clusters of connected pixels are color-coded with warm or cold colors depending on the belonging to the dark or bright phase in the BSE micrographs, respectively.

If both phases are completely disordered or if at least one of the phases is ordered was investigated by means of diffraction experiments. Due to the insufficient dynamic range of laboratory X-ray diffraction methods to distinguish the A2 from the B2 crystal structure [19], transmission electron experiments were performed. Selected area diffraction (SAD) reveals characteristic superlattice diffraction spots corresponding to the B2 crystal structure as depicted in in Fig. 4 a) and b) for the respective alloys. For the SAD from 82(TaMoTi)-8Cr-10Al selected spots corresponding to the B2 crystal structure are labeled in red in Fig. 4 a). Both alloys show the same set of diffraction spots. This confirms the FactSage prediction of a B2 crystal structure present at room temperature.

Micrographs in Dark-Field (DF) mode on (100) B2 spots were taken to distinguish between ordered and disordered regions. Due to the DF imaging, B2 appears bright and A2 dark in the micrographs. In case of the 82(TaMoTi)-8Cr-10Al alloy, the matrix phase can be assigned A2 while the precipitates exhibit a B2 crystal structure as displayed in Fig. 4 c). It might have been possible, based on the large number of constituent elements, that the given contrast variation is a result of different levels of ordering of the B2 phase. However, this would then have resulted in more distinct superlattice spots seen in Fig. 4 a) and should not lead to a contrast variation in the high-angle annular dark-field, which yields an atomic contrast (displayed in Supplemental Fig. S4). Such a contrast is seen in the STEM-HAADF micrographs and confirmed by STEM-EDS as depicted in Fig. 4 c). Correspondingly, the contrast variation seen in the DF images is solely linked to distinguishing the ordered and disordered phases. The above-discussed type of difference in contrast between ordered and disordered phases at such length scales has also previously been reported in Refs. [26, 43, 44]. In case of 82(TaMoTi)-8Cr-10Al, the matrix phase is enriched in Ta and Mo while the concentration of Ti and Al is reduced with respect to the mean concentration. The precipitates exhibit a high concentration of Ti and Al while being depleted in Ta and Mo. No significant segregation of Cr was observed. The precipitates seem to be uniformly distributed within the investigated region. This observation confirms the SEM results, which indicated such a microstructure.

The 77(TaMoTi)-8Cr-15Al alloy exhibits a more complex microstructure, as anticipated from the SEM investigations (see Fig. 3 b)). The TEM-DF micrographs depicted in Fig. 4 d) exhibit a microstructure consisting of loop features and cuboidal precipitates. The continuous matrix phase appears bright in the dark-field mode and is, therefore, B2 while the cuboidal precipitates are A2. With respect to the matrix, the loops and precipitates are enriched in Ta and Mo and depleted in Ti and Al as confirmed by STEM-EDS. Similar to 82(TaMoTi)-8Cr-10Al, Cr does not substantially partition.

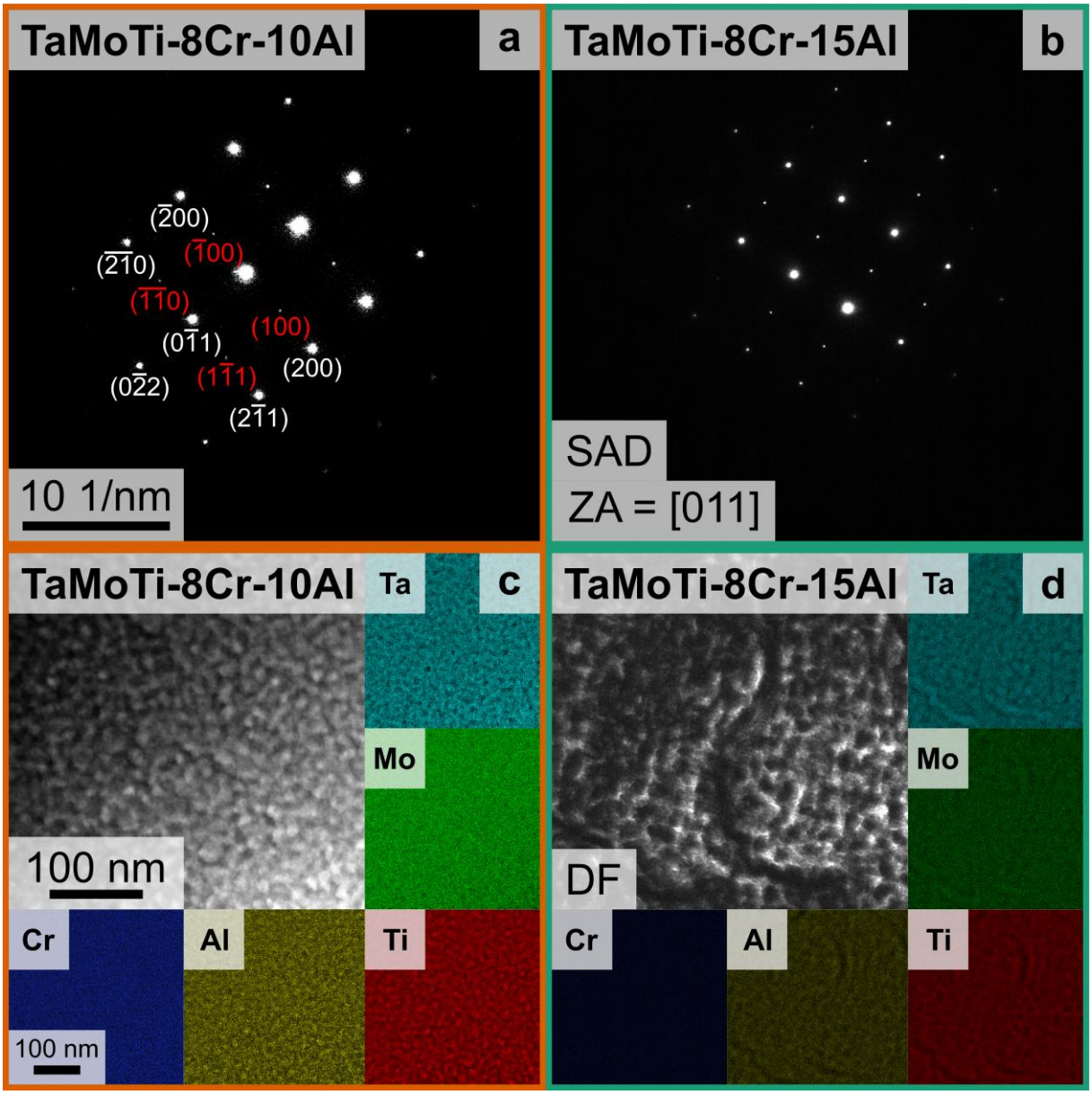

Fig. 4. TEM-SAD patterns of: a) 82(TaMoTi)-8Cr-10Al and b) 77(TaMoTi)-8Cr-15Al. In a) selected spots corresponding to the B2 crystal structure are labeled in red and some spots corresponding to the A2 crystal structure are labeled in white. For detailed description, the reader is referred to the text. Both patterns are acquired close to the [011] zone axis (ZA) and at the same camera length. TEM-DF micrographs with their respective element maps by STEM-EDS are shown for: c) 82(TaMoTi)-8Cr-10Al and d) 77(TaMoTi)-8Cr-15Al. The respective element maps display the same field of view as the TEM-DF micrographs. The TEM-DF micrographs were taken with the objective aperture on the (100) B2 spot. c) and d) are taken at the same magnification.

After confirming the chemical composition and macroscopic microstructure, the samples were further investigated utilizing DSC. Various heating and cooling rates were employed to distinguish between the different possible transitions and depicted in Fig. 5 [40, 37]. 82(TaMoTi)-8Cr-10Al exhibits a single peak in the $\mathrm{d}H/\mathrm{d}T$ curve (highlighted in Fig. 5 a) by an inverted triangle). For the aforementioned conditions, the peak is sensitive to the different heating rates with peak temperatures at 1055, 1062 and 1073 °C for 10, 20 and 40 K/min, respectively (depicted in Fig. 5 c)). Furthermore, the peak shape is almost symmetrical; however, a slightly steeper decline to higher temperatures is noted. Similar shapes, peak temperatures and tendencies are recorded while cooling from high temperatures (not shown here).

In contrast, 77(TaMoTi)-8Cr-15Al exhibits overlapping peaks. Therefore, a complex phase transition is expected. These broad peaks are separated by roughly 40 – 60 K, dependent on the heating and cooling

rate. The peak at lower temperatures (indicated by a hexagon) is at 1096, 1104 and 1115 °C for 10, 20 and 40 K/min, respectively. The changing peak temperature indicates a heating rate sensitivity. The high temperature peak marked by a diamond-shaped symbol in Fig. 5 b) is at 1155, 1157 and 1155 °C for 10, 20 and 40 K/min, respectively. Due to the peak temperature change of only 2 K, it can be regarded as temperature insensitive, as displayed in detail in Fig. 5 c). The signal exhibits a steep decline to higher temperatures at the second peak (diamond symbol). In the ascending and descending $\mathrm{d}H/\mathrm{d}T$ slopes (below and above both peak temperatures), the curves feature a change in the slope and the point of deflection is highlighted by an arrow in Fig. 5 b).

To assess $\mathrm{d}H/\mathrm{d}T$ signals, the peak shape and symmetry as well as the dependence on the heating rate have to be considered. During heating, a $\mathrm{d}H/\mathrm{d}T$ peak corresponding to a discontinuous transition (e.g., melting or freezing of a pure material under ideal conditions) exhibits a nearly symmetric shape with a linear portion until reaching the maximum, followed by an exponential return to the baseline [40]. Diffusion-based processes, as nucleation and growth (precipitation) or spinodal decomposition, require long-range atomic diffusion and therefore exhibit a strong temperature dependence [38, 45]. A continuous transition without diffusion (e.g., ordering transitions) on the other hand features an exponential increase and an abrupt decline to the baseline after the peak temperature, typically referred to as a “lambda”-peak, because of the resemblance to the Greek letter, λ [36, 37]. This is due to only localized atomic rearrangements within a unit cell during the ordering transition [36, 37]. This is the nature of the peaks marked by the diamond in Fig. 5 b). The slight difference in the experimentally determined peak temperatures (variation of 2 K) is because of a combination of thermal lag in the calorimeter and kinetic lag due to simultaneous diffusion processes [40].

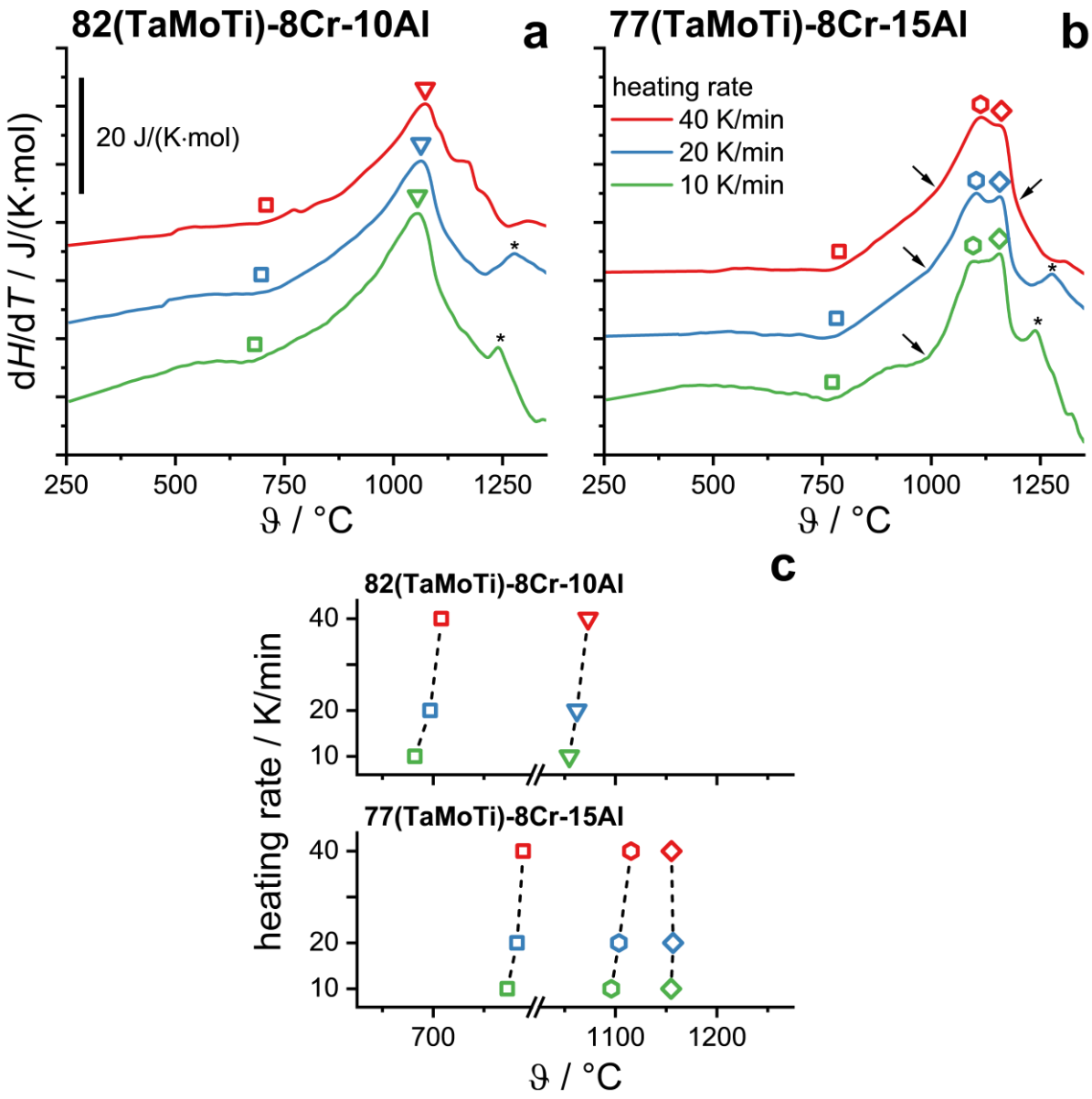

Fig. 5. Derivate of enthalpy with respect to temperature dH/dT of: a) 82(TaMoTi)-8Cr-10Al and b) 77(TaMoTi)-8Cr-15Al. The signals are offset in order to allow interpretation of otherwise overlapping curves. DSC was performed with heating rates of 10, 20 and 40 K/min in a Zr-gettered Ar atmosphere. Onsets are marked by square symbols, while distinct peaks are marked by an inverted triangle (for 82(TaMoTi)-8Cr-10Al), hexagon and diamond (for 77(TaMoTi)-8Cr-15Al). c) Onset and peak temperature as a function of heating rate for the investigated alloys. Please note that the dotted lines are to guide the eyes. The same symbols are used throughout the figure. Scaling and color code is the same in image a) and b). Artifacts arising due to measurement errors are marked by *.

Based on the critical temperatures determined from the DSC experiments, both compositions were water quenched from lower (1000 °C) and higher (1200 °C) temperatures compared to the experimental peak temperatures. The corresponding SEM-BSE micrographs for both alloys and temperatures are displayed in Fig. 6. After the quenching from 1000 °C, 82(TaMoTi)-8Cr-10Al exhibits a similar microstructure as after the furnace cooling. The dark precipitates (by BSE contrast imaging) are 10 – 30 nm in size and of spherical shape (see Fig. 6 a)). Quenching to RT from 1200 °C leads to no Z-contrast in the micrographs in Fig. 6 c) (only orientation contrast from grain orientation, not shown here). The microstructure of 77(TaMoTi)-8Cr-15Al after quenching from 1000 °C to RT is similar to post furnace cooling whereas subsequent to quenching from 1200 °C, no precipitates are obtained by SEM-BSE imaging. Though, fine loops with a high BSE contrast are observed.

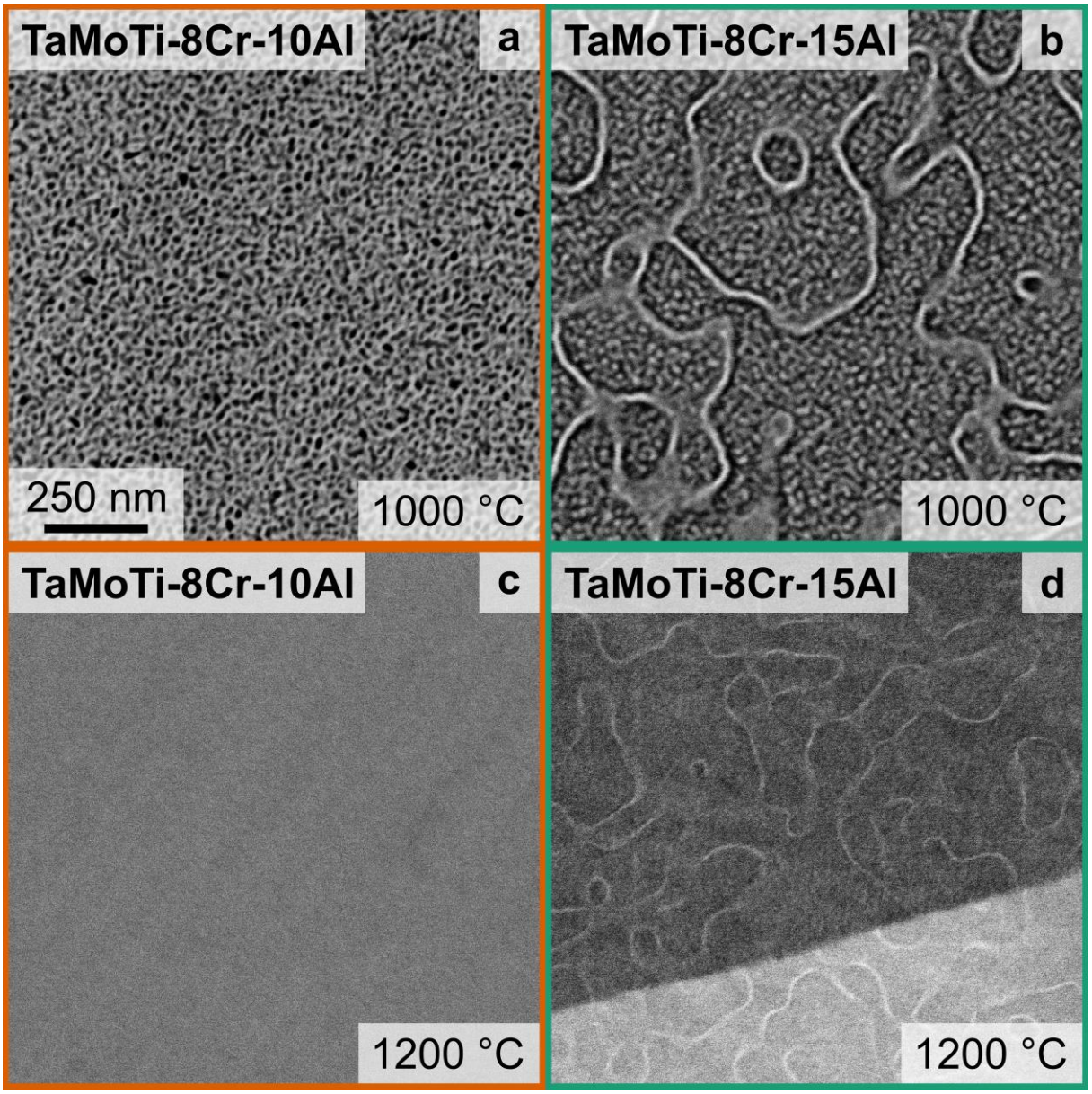

Fig. 6. BSE micrographs of a,c) 82(TaMoTi)-8Cr-10Al and b,d) 77(TaMoTi)-8Cr-15Al (right) after water quenching following a heat treatment of 30 min at a,b) 1000 °C and c,d) 1200 °C. The micrographs were taken at the same magnification.

5 Discussion

5.1. Phase separation with concurrent ordering

In the present case of 82(TaMoTi)-8Cr-10Al, the thermoanalytical dataset indicates that the phase separation and ordering occur at or almost the same temperature. By quenching, a supersaturated solid solution is achieved in this system (see Fig. 6 c)). This result and the heating rate dependence of the onset and peak measured by DSC indicates a bulk diffusion controlled discontinuous phase transition. No signature of the ordering of the second phase is observed by means of DSC. Hence, the formation of the ordered second phase from the supersaturated concentrated solid solution is through concomitant clustering and ordering. Therefore, a sequence of α with A2 crystal structure to $\alpha + \beta'$ is expected with β' being of B2 crystal structure and significantly different chemical composition. α forms a disordered,

continuous matrix while β' serves as ordered precipitates. Due to this characteristic morphology, a spinodal decomposition is unlikely.

5.2. Preceding ordering followed by phase separation

The Al-rich alloy exhibits a microstructure, which can be divided into two features which will be discussed separately: the loop-like features and the cuboidal precipitates.

The loop-like feature observed in the 77(TaMoTi)-8Cr-15Al sample are at a first glance similar to thermal anti-phase domain boundaries, which separate adjacent ordered domains. These are known from ordered compounds, like NiAl [46] and TiAl [47, 35, 48] and were recently reported in B2 RCCA [19, 49]. In case of 77(TaMoTi)-8Cr-15Al, it seems like these planar faults exhibit a lower degree of order (as they appear darker than the matrix phase in the TEM-DF images) and Mo and Ta segregate to them, as shown in the EDS mappings in Fig. 4 d). After quenching from 1200 °C, the planar faults are significantly thinner, indicative of a reduced amount of segregated Mo and Ta. Similar findings were reported by Chen et al. [19] for the equimolar TaMoTiCrAl and MoCrTiAl and have been related to the phase transition from the high-temperature A2 crystal structure to the low temperature B2 crystal structure. Therefore, the presence of planar faults in 77(TaMoTi)-8Cr-15Al is indicative of an ordering transition. This is in perfect agreement with the DSC results, which exhibit a heating rate insensitive λ-shaped peak at 1155 °C. The size of the domains is small in comparison with the equimolar TaMoTiCrAl. This may be due to the small temperature gap (approx. 50 K) between the order transition and the onset of the phase separation. Another possibility could be slow kinetics due to low T_c insufficient to facilitate significant growth. A possible continuous order parameter would be the consistently increasing degree of occupation at a given lattice site in the B2 crystal structure, as discussed beforehand.

The phase separation, resulting in the cuboidal precipitates is expected approximately 50 K below the order-disorder transition of the matrix (determined by the $\mathrm{d}H/\mathrm{d}T$ peak temperature). No additional $\mathrm{d}H/\mathrm{d}T$ signal at even lower temperatures is observed. Further, no change in the microstructure (with respect to the furnace cooled condition) is determined after the quenching from 1000 °C. Therefore, it is expected that the precipitates are formed directly with a disordered crystal. The $\mathrm{d}H/\mathrm{d}T$ signal of the phase separation exhibits a heating rate dependency, which is typical of diffusion-based processes. Accordingly, this phase separation was suppressed by water quenching from 1200 °C to RT (see Fig. 6 d)). Hence, the following phase transition is expected $\alpha \rightarrow \alpha' \rightarrow \alpha' + \beta$. β serves as disordered precipitates, homogenously formed within the continuous and ordered matrix α'. Again, a spinodal decomposition is unlikely for this characteristic morphology. If the segregation to the anti-phase domain boundaries results from the aforementioned phase separation cannot be concluded from this study and a third reaction remains possible. In the case of the quenching experiment from 1200 °C with remaining loop-like features, the dwell time of 30 min might not have been sufficient to homogenize the segregations from the furnace-cooled condition.

5.3. Generalization

A similar microstructure as 77(TaMoTi)-8Cr-15Al was reported by Schliephake et al. [43] for the 85(TaMoTi)-15Al alloy (after homogenization and aging heat treatment). Segregation at planar faults and cuboidal, disordered precipitates were also observed there. The composition in Ref. [43] is similar with respect to Ta, Mo, Ti and Al; however, the alloy is free of Cr. This strengthens the assumption based on thermodynamic calculations [31], that the interplay between the A2 forming elements (Ta, Mo and Cr) and Al promotes the order reaction significantly. However, the exact impact of Cr on ordering is still elusive. Thermodynamic calculations predict significant participation in the B2 phase (see

Supplemental Fig. S2), while a uniform distribution is determined by TEM (see Fig. 4 c) and d)). This could indicate, that the samples are not in a thermodynamic equilibrium state after cooling inside the furnace.

Similar findings were also reported for ternary systems, which combine various refractory metals with Al. For example, some alloys from the ternary systems Ti-Al-X (with X = Ta, Nb and Mo) exhibit B2 crystal structure at room temperature even after fast cooling at 10^5 – 10^6 K/s [47]. Whitfield et al. [50] investigated the effect of Al concentration on the phase separation and ordering within the system $(100 - x)$(TiTaZr)-xAl and reported that Al promotes the occurrence of order. In this case, quenched alloys with more than 10 at.% Al exhibited a B2 phase, while those with 0 or 5 at.% Al did not feature superlattice spots in their respective SAD pattern. Notwithstanding that their thermal analysis (with a heating rate of 10 K/min) indicated an order-disorder transition at approximately 650 °C for the Al-lean alloy with 5 at.%. It should be noted, that a phase separation (presumably spinodal decomposition) in this composition is reported at higher temperatures than the order transition.

To summarize, a schematic phase diagram is depicted in Fig. 7. Most of the reported RCCA and HEA exhibit phase transitions as marked by line I or line IV. When optimizing the composition, the question arises whether there is a two-phase field (or if $x_1 = x_3$) and where x_1 and x_3 are located in relation to x_2. Only for few reported RCCA systems, the influence of the Al concentration was systematically investigated. However, in most cases it appears that $x_1 \approx x_2$. Therefore, the majority of reported two-phase RCCA resemble line III, while line II is preferred to achieve a two-phase microstructure with a disordered matrix. Apart from the reaction sequence, it should be pointed out that for high-temperature structural applications (e.g., creep), solvus temperature, vacancy formation enthalpy and interface properties of the precipitates are of major importance as well. In the present case, the alloys 82(TaMoTi)-8Cr-10Al and 77(TaMoTi)-8Cr-15Al correspond to lines II and III, respectively. If the ordering is mediated through a continuous transition, the high-temperature crystal structure (A2) cannot be retained until room temperature through fast cooling or quenching because no energetic barrier exists [37, 47].

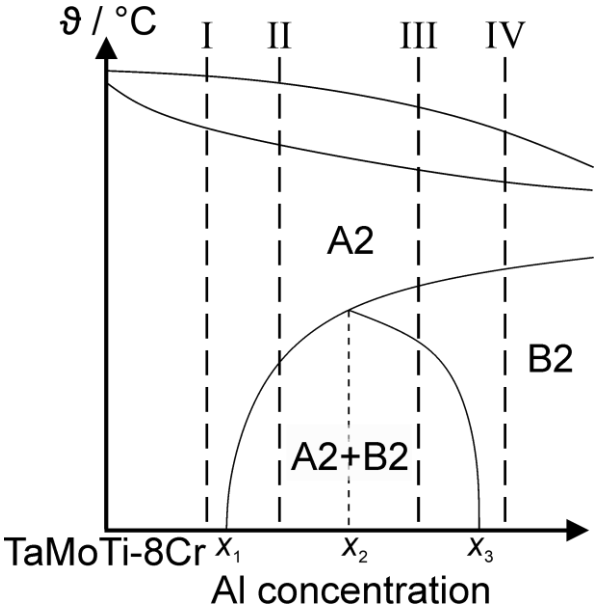

Fig. 7. Schematic phase diagram, after Ref. [35].

Due to the relatively high transition temperatures (being significantly over 1000 °C), this alloy system may be a good candidate for high temperature structural applications. The fact that a disordered matrix

is attained after slow cooling leaves potential for further improvement with respect to possible promising high temperature mechanical properties.

6 Conclusions

Thermodynamic calculations performed in FactSage with an in-house database predicted the equilibrium phases at room temperature from the quasi-binary system (100-x_{Al})(TaMoTi)-8Cr-x_{Al}Al (in at.%). For $x_{\mathrm{Al}} > 2.5$ at.%, a two-phase microstructure consisting of A2 and B2 exists according to these calculations. Additionally, a single-phase B2 crystal structure is expected for $x_{\mathrm{Al}} > 12.5$ at.% at intermediate temperatures (approx. 700 – 1200 °C). Thermal analysis and post mortem electron imaging were utilized to ascertain the characteristics of the phase transitions within this system.

In case of 82(TaMoTi)-8Cr-10Al, a single concurrent phase separation as well as an order reaction was determined to take place. This phase separation exhibits a maximum reaction rate at (1055 – 1073) °C for 10 – 40 K/min and a lower onset temperature of approx. 750 °C. The reaction leads to small cuboidal B2 precipitates in a continuous A2 matrix at room temperature after furnace cooling. The phase separation can be suppressed by water quenching from 1200 °C. The diffusion controlled precipitation reaction $\alpha \rightarrow \alpha + \beta'$ is therefore proposed (α is A2, β' is B2).

On the other hand, the 77(TaMoTi)-8Cr-15Al alloy exhibits a continuous phase transition from A2 to B2 at 1155 °C. At lower temperatures, a phase separation is determined with a $\mathrm{d}H/\mathrm{d}T$ maximum at 1096 – 1115 °C for 10 – 40 K/min. This results in cuboidal A2 precipitates within a B2 matrix at room temperature. Segregated planar faults are present in this alloy, similar to the former single-phase B2 crystal structure. The B2 domains are comparatively small (in the range of a few hundred nm), indicative of a small temperature gap between the phase transition and subsequent phase separation or slow kinetics due to low T_{c}. The continuous phase transition is not constrained by heating or cooling rate. The following sequence is suggested $\alpha \rightarrow \alpha' \rightarrow \alpha' + \beta$ (α and β are A2, α' is B2).

In both investigated alloys, the A2 phase is enriched in Ta and Mo, while the B2 phase is enriched in Ti and Al. The minor amount of Cr seems to be uniformly distributed. In summation, Al seems to promote the formation of B2 order in the alloy system Ta-Mo-Ti-Cr-Al. At low concentrations (approx. 5 – 12.5 at.%), only precipitates are enriched in Al and exhibit the B2 crystal structure while at intermediate concentrations of Al (approx. 12.5 – 20 at.%), the matrix is ordered. However, a disordered second phase, depleted in Al forms as precipitates. In case of even higher Al concentrations, a single-phase B2 matrix is reported [19].

Hence, the sequence of phase separation and ordering can be controlled by adjusting the composition ratio of Al to refractory A2-forming element in the Ta-Mo-Ti-Cr-Al system. Thus, a pursued microstructure composed of a potentially ductile A2 matrix with B2 precipitates can be achieved in a wide composition range within this alloy system. The present study serves as a firm foundation as far as alloy design of a two-phase material for high-temperature structural applications is concerned. Specifically, the wide alloying range in the system provides significant opportunity to further improve the desired high-temperature properties through specific compositional adjustment and heat treatment strategies. This includes optimization of the composition to maximize the solid solution strengthening of the matrix. Additionally, creep resistance might be enhanced by increasing the critical temperature of phase separation, adjusting A2+B2 phase distribution as well as size and shape of precipitates. Composition and microstructure also play a significant role in case of the oxidation resistance. In this way, a targeted effort can be made by understanding the sequence of microstructural evolution, phase

493 transitions as well as ordering involved, to obtain a suitable microstructure for high-temperature
494 structural applications.

495 Acknowledgments

496 The financial support by the Deutsche Forschungsgemeinschaft (DFG), grant no. HE 1872/34-2 is
497 gratefully acknowledged. The authors acknowledge the chemical analysis by ICP-OES at the Institute
498 for Applied Materials (IAM-AWP), Karlsruhe Institute of Technology (KIT). Part of this work was
499 performed at the Micro- and Nanoanalytics Facility (MNaF) of the University of Siegen. The authors
500 thank J. Müller from the Micro- and Nanoanalysis & - tomography group (University of Siegen) for his
501 assistance in TEM observation. We would like to express our gratitude to C. Greiner (KIT IAM-CMS
502 MicroTribology Centrum μTC) for supporting the electron microscopy work. We also thank B.-
503 D. Nguyen, L. Wengenmayer, C. Sax and D. Probst for experimental support. The authors thank
504 H. Chen, C. Schulz and F. Müller for fruitful discussions.

7 References

505

[1] D. B. Miracle and O. N. Senkov, "A critical review of high entropy alloys and related concepts," *Acta Materialia,* vol. 122, pp. 448-511, 2017.

[2] D. B. Miracle, M. H. Tsai, O. N. Senkov, V. Soni and R. Banerjee, "Refractory high entropy superalloys (RSAs)," *Scripta Materialia,* vol. 187, pp. 445-452, 2020.

[3] O. N. Senkov, D. B. Miracle, K. J. Chaput and J.-P. Couzinié, "Development and exploration of refractory high entropy alloys - A review," *Journal of Materials Research,* vol. 33, no. 19, pp. 3092-3128, 2018.

[4] S. Gorsse, J.-P. Couzinié and D. B. Miracle, "From high-entropy alloys to complex concentrated alloys," *Comptes Rendus Physique,* vol. 19, pp. 721-736, 2018.

[5] J.-W. Yeh, S.-K. Chen, S.-J. Lin, J.-Y. Gan, T.-S. Chin, T.-T. Shun, C.-H. Tsau and S.-Y. Chang, "Nanostructured High-Entropy Alloys with Multiple Principal Elements: Novel Alloy Design Concepts and Outcomes," *Advanced Engineering Materials,* vol. 5, no. 6, pp. 299-303, 2004.

[6] O. N. Senkov, G. B. Wilks, D. B. Miracle, C. P. Chuang and P. K. Liaw, "Refractory high-entropy alloys," *Intermetallics,* vol. 18, pp. 1758-1765, 2010.

[7] O. N. Senkov, G. B. Wilks, J. M. Scott and D. B. Miracle, "Mechanical properties of Nb25Mo25Ta25W25 and V20Nb20Mo20Ta20W20 refractory high entropy alloys," *Intermetallics,* vol. 19, pp. 698-706, 2011.

[8] J. R. DiStefano, B. A. Pint and J. H. DeVan, "Oxidation of refractory metals in air and low pressure oxygen gas," *International Journal of Refractory Metals & Hard Materials,* vol. 18, pp. 237-243, 2000.

[9] O. N. Senkov, S. V. Senkova, D. M. Dimiduk, C. Woodward and D. B. Miracle, "Oxidation behavior of a refractory NbCrMo0.5Ta0.5TiZr alloy," *Journal of Materials Science,* vol. 47, pp. 6522-6534, 2012.

[10] B. Gorr, S. Schellert, F. Müller, H.-J. Christ, A. Kauffmann and M. Heilmaier, "Current Status of Research on the Oxidation Behavior of Refractory High Entropy Alloys," *Advanced Engineering Materials,* no. 2001047, p. 2001047, 2021.

[11] B. Gorr, F. Müller, S. Schellert, H.-J. Christ, H. Chen, A. Kauffmann and M. Heilmaier, "A new strategy to intrinsically protect refractory metal based alloys at ultra high temperatures," *Corrosion Science,* vol. 166, p. 108475, 2020.

[12] S. Schellert, B. Gorr, H.-J. Christ, C. Pritzel, S. Laube, A. Kauffmann and M. Heilmaier, "The Effect of Al on the Formation of a CrTaO4 Layer in Refractory High Entropy Alloys Ta-Mo-Cr-Ti-xAl," *Oxidation of Metals,* pp. 1-13, 2021.

[13] S. Gorsse, D. B. Miracle and O. N. Senkov, "Mapping the world of complex concentrated alloys," *Acta Materialia,* no. 135, pp. 177-187, 2017.

[14] B. Gorr, M. Azim, H.-J. Christ, T. Müller, D. Schliephake and M. Heilmaier, "Phase equilibria, microstructure, and high temperature oxidation resistance of novel refractory high-entropy alloys," *Journal of Alloys and Compounds,* vol. 624, pp. 270-278, 2015.

[15] F. Müller, B. Gorr, H.-J. Christ, J. Müller, B. Butz, H. Chen, A. Kauffmann and M. Heilmaier, "On the oxidation mechanism of refractory high entropy alloys," *Corrosion Science,* vol. 159, p. 108161, 2019.

[16] M. Ghadyani, C. Utton and P. Tsakiropoulos, "Microstructures and Isothermal Oxidation of the Alumina Scale Forming Nb1.45Si2.7Ti2.25Al3.25Hf0.35 and Nb1.35Si2.3Ti2.3Al3.7Hf0.35 alloy," *materials,* vol. 5, no. 12, p. 759, 2019.

[17] K.-C. Lo, Y.-J. Chang, H. Murakami, J.-W. Yeh and A.-C. Yeh, "An oxidation resistant refractory high entropy alloy protected by CrTaO4-based oxide," *scientific reports,* no. 9, p. 7266, 2019.

[18] S. Laube, H. Chen, A. Kauffmann, S. Schellert, F. Müller, B. Gorr, J. Müller, B. Butz, H.-J. Christ and M. Heilmaier, "Controlling crystallographic ordering in Mo-Cr-Ti-Al high entropy alloys to enhance ductility," *Journal of Alloys and Compounds,* vol. 823, p. 153805, 2020.

[19] H. Chen, A. Kauffmann, S. Seils, T. Boll, C. H. Liebscher, I. Harding, K. S. Kumar, D. V. Szabó, S. Schlabach, S. Kauffmann-Weiss, F. Müller, B. Gorr, H.-J. Christ and M. Heilmaier, "Crystallographic ordering in a series of Al-containing refractory high entropy alloys Ta-Nb-Mo-Cr-Ti-Al," *Acta Materialia,* vol. 176, pp. 123-133, 2019.

[20] O. N. Senkov, S. V. Senkova and C. Woordward, "Effect of aluminum on the microstructure and properties of two refractory high-entropy alloys," *Acta Materialia,* vol. 68, pp. 214-228, 2014.

[21] T. M. Pollock and S. Tin, "Nickel-Based Superalloys for Advanced Turbine Engines: Chemistry, Microstructure, and Properties," *Journal of Propulsion and Power,* vol. 22, no. 2, pp. 361-374, 2006.

[22] L. J. Santodonato, Y. Zhang, M. Feygenson, C. M. Parish, M. C. Gao, R. J. Weber, J. C. Neuefeind, Z. Tang and P. K. Liaw, "Deviation from high-entropy configurations in the atomic distributions of a multi-principal-element alloy," *Nature Communications,* vol. 6, p. 5964, 2015.

[23] L. J. Santodonato, P. K. Liaw, R. R. Unocic, H. Bei and J. R. Morris, "Predictive multiphase evolution in Al-containing high-entropy alloys," *Nature Communications,* vol. 9, p. 4520, 2018.

[24] J. K. Jensen, B. A. Welk, R. E. Williams, J. M. Sosa, D. E. Huber, O. N. Senkov, G. B. Viswanathan and H. L. Fraser, "Characterization of the microstructure of the compositionally complex alloy AlMo0.5NbTa0.5TiZr," *Scripta Materialia,* vol. 121, pp. 1-4, 2016.

[25] O. N. Senkov, C. Woodward and D. B. Miracle, "Microstructure and Properties of Aluminum-Containing Refractory High-Entropy Alloys," *JOM,* vol. 66, no. 10, pp. 2030-2042, 2014.

[26] V. Soni, B. Gwalani, T. Alam, S. Dasari, Y. Zheng, O. N. Senkov, D. Miracle and R. Banerjee, "Phase inversion in a two-phase, BCC+B2, refractory high entropy alloy," *Acta Materialia,* vol. 185, pp. 89-97, 2020.

[27] H. Okamoto, M. E. Schlesinger and E. M. Mueller, ASM Handbook Volume 3: Alloy Phase Diagrams, Materials Park, Ohio: ASM International, 2016.

[28] E. Rudy, Ternary Phase Equilibria in Transition Metal-Boron-Carbon-Silicon Systems, Wright-Patterson Air Force Base, Ohio: Air Force Material Laboratory, 1969.

[29] T. Helander and O. Tolochko, "An Experimental Investigation of Possible B2-Ordering in the Al-Cr System," *Journal of Phase Equilibria,* vol. 1, no. 20, pp. 57-60, 1999.

[30] N. Saunders and Thermotech Ltd., "The Al-Mo System (Aluminum-Molybdenum," *Journal of Phase Equilibria,* vol. 4, no. 18, pp. 370-378, 1997.

[31] F. Müller, B. Gorr, H.-J. Christ, H. Chen, A. Kauffmann, S. Laube and M. Heilmaier, "Formation of complex intermetallic phases in novel refractory high-entropy alloys NbMoCrTiAl and TaMoCrTiAl - Thermodynamic assessment and experimental validation," *Journal of Alloys and Compounds,* vol. 842, p. 155726, 2020.

[32] N. Yurchenko, N. Stepanov and G. Salishchev, "Laves-phase formation criterion for high-entropy alloys," *Materials Science and Technology,* vol. 33, no. 1, pp. 17-22, 2017.

[33] D. P. Pishchur and V. A. Drebushchak, "Recommendations on DSC calibration," *Journal of Thermal Analysis and Calorimetry,* vol. 124, pp. 951-958, 2016.

[34] H. Chen, A. Kauffmann, S. Laube, I.-C. Choi, R. Schwaiger, Y. Huang, K. Lichtenberg, F. Müller, B. Gorr, H.-J. Christ and M. Heilmaier, "Contribution of Lattice Distortion to Solid Solution Strengthening in a Series of Refractory High Entropy Alloys," *Metallurgical and Materials Transactions A,* vol. 49, pp. 772-781, 2017.

[35] S. Naka and T. Khan, "Designing novel multiconstituent intermetallics: Contribution of modern alloy theory in developing engineered materials," *Journal of Phase Equilibria,* vol. 18, no. 6, p. 635, 1997.

[36] V. Raghavan and M. Cohen, "Solid-State Phase Transformations," in *Changes of State*, vol. 5, Bosten, MA., Springer, 1975.

[37] D. A. Porter, K. E. Easterling and M. Y. Sherif, Phase Transformations in Metals and Alloys, Boca Raton: CRC Press, 2009.

[38] W. A. Soffa and D. E. Laughlin, "Decomposition and ordering processes involving thermodynamically first-order order → disorder transformations," *Acta Metallurgica,* vol. 37, no. 11, pp. 3019-3028, 1989.

[39] R. A. Cowley, "Structural phase transitions I. Landau theory," *Advances in Physics,* vol. 29, no. 1, pp. 1-110, 1980.

[40] W. J. Boettinger, U. R. Kattner, K.-W. Moon and J. H. Perepezko, DTA and Heat-flux DSC Measurements of Alloy Melting and Freezing, Washington: National Institute of Standards and Technology, 2006.

[41] R. W. Balluffi and L. L. Seigle, "Growth of voids in metals during diffusion and creep," *Acta Metallurgica,* vol. 5, pp. 449-454, 1957.

[42] S. Oberst, A. Kauffmann, S. Seils, S. Schellert, M. Weber, B. Gorr, H.-J. Christ. and M. Heilmaier, "On the chemical and microstructural requirements for the pesting-resistance of Mo-Si-Ti alloys," *Journal of Materials Research and Technology,* vol. 9, no. 4, pp. 8556-8567, 2020.

[43] D. Schliephake, A. E. Medvedev, M. K. Imran, S. Obert, D. Fabijanic, M. Heilmaier, A. Molotnikov and X. Wu, "Precipitation behaviour and mechanical properties of a novel Al0.5MoTaTi complex concentrated alloy," *Scripta Materialia,* vol. 173, pp. 16-20, 2019.

[44] V. Soni, B. Gwalani, O. N. Senkov, B. Viswanathan, T. Alam, D. B. Miracle and R. Banerjee, "Phase stability as a function of temperature in a refractory high-entropy alloy," *Journal of Materials Research,* vol. 33, no. 19, pp. 3235-3246, 2018.

[45] J.-C. Zhao and M. R. Notis, "Spinodal decomposition, ordering transformation, and discontinuous precipitation in a Cu–15Ni–8Sn alloy," *Acta Materialia,* vol. 46, no. 12, pp. 4203-4218, 1998.

[46] D. B. Miracle, "The physical and mechanical properties of NiAl," *Acta Metallurgica et Materialia,* vol. 41, no. 3, pp. 649-684, 1993.

[47] K. Das and S. Das, "Order-disorder transformation of the body centered cubic phase in the Ti-Al-X (X=Ta, Nb, or Mo) system," *Journal of Materials Science,* vol. 38, p. 3995 – 4002, 2003.

[48] Y. G. Li, P. A. Blenkinsop, M. H. Loretto and N. A. Walker, "Effect of aluminiumon ordering of highly stabilised β-Ti-V-Cr alloys," *Materials Science and Technology,* vol. 14, no. 8, pp. 732-737, 1998.

[49] N. Y. Yurchenko, N. D. Stepanov, S. V. Zherebtsov, M. A. Tikhonovsky and G. A. Salishchev, "Structure and mechanical properties of B2 ordered refractory AlNbTiVZrx (x = 0-1.5) high-entropy alloys," *Materials Science & Engineering A,* vol. 704, pp. 82-90, 2017.

[50] T. E. Whitfield, E. J. Pickering, L. R. Owen, C. N. Jones, H. J. Stone and N. G. Jones, "The effect of Al on the formation and stability of a BCC – B2 microstructure in a refractory metal high entropy superalloy system," *Materialia,* vol. 13, p. 100858, 2020.

506

507